Distance-Dependent Plasmon-Enhanced Singlet Oxygen Production and Emission for Bacterial Inactivation

Oriol Planas,[‡,§] Nicolas Macia,[†,§] Montserrat Agut,[‡] Santi Nonell,*,[‡,§] and Belinda Heyne*,[†,§]

[†]Department of Chemistry, University of Calgary, Alberta AB T2N 1N4, Canada
[‡]Institut Quimic de Sarria, Universitat Ramon Llull, Barcelona 08022, Spain

S *Supporting Information*

ABSTRACT: Herein, we synthesized a series of 10 core–shell silver–silica nanoparticles with a photosensitizer, Rose Bengal, tethered to their surface. Each nanoparticle possesses an identical silver core of about 67 nm, but presents a different silica shell thickness ranging from 5 to 100 nm. These hybrid plasmonic nanoparticles thus afford a plasmonic nanostructure platform with a source of singlet oxygen ($^1O_2$) at a well-defined distance from the metallic core. Via time-resolved and steady state spectroscopic techniques, we demonstrate the silver core exerts a dual role of enhancing both the production of $^1O_2$, through enhanced absorption of light, and its radiative decay, which in turn boosts $^1O_2$ phosphorescence emission to a greater extent. Furthermore, we show both the production and emission of $^1O_2$ *in vitro* to be dependent on proximity to the plasmonic nanostructure. Our results clearly exhibit three distinct regimes as the plasmonic nanostructure moves apart from the $^1O_2$ source, with a greater enhancement for silica shell thicknesses ranging between 10 and 20 nm. Moreover, these hybrid plasmonic nanoparticles can be delivered to both Gram-positive and Gram-negative bacteria boosting both photoantibacterial activity and detection limit of $^1O_2$ in cells.
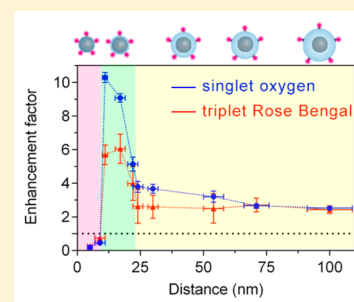
INTRODUCTION

In the past decade, metallic nanoparticles, also known as plasmonic nanoparticles, have been exploited for their intrinsic ability to concentrate the light intensity they absorb over a small region in space near their surface.[1] This phenomenon can be understood conceptually as the many electrons of the nanoparticle's conduction band start to oscillate collectively upon interaction with an incident beam of appropriate energy.[1,2] While all the electrons are assumed to participate in this collective process, only the surface of the metallic nanoparticle experiences an oscillating charge, which corresponds to the surface plasmon.[1] The considerable strength of this oscillating field is identified by the large molar extinction coefficients exhibited by metallic nanoparticles, which are at least several orders of magnitude greater than values reported for molecular structures.[1a,3] Therefore, excited plasmonic nanoparticles play the role of antennas where nearby molecules are exposed to greater light intensity. Such effects result in an enhancement of a variety of optical processes near the metallic nanoparticle surface. Modification of photoprocesses, such as vibrational transitions (SERS), absorption, and emission (fluorescence and phosphorescence), is well documented.[4]

Because the local field at the surface of the metallic nanoparticle behaves as an evanescent wave and is of very short duration[5] (only few femtoseconds), plasmon-enhanced phenomena are distance dependent, affecting only the molecules which reside in the region of the surface plasmon at the time of light absorption.[1a,6] At very short distances, efficient quenching of molecular transitions by nanoparticles occurs, whereas excited metallic nanoparticles have absolutely no influence on their surrounding at very long distances.[1a,7] It is in the intermediate distances that enhancement takes place, resulting from the plasmon–dipole interaction between the excited plasmonic nanoparticles and the nearby molecules.[1a,7] This resonant coupling affects not only the excitation of neighboring molecules but also their emission quantum yield as an increase in radiative decay rate is observed near the surface of the metallic nanoparticles.[1a,4c,6a] So far, the strongest enhancements have been reported for molecules located within 10−20 nm from the plasmonic surface.[6a,b]

Singlet oxygen ($^1O_2$), corresponding to the lowest-lying electronic excited state of molecular oxygen, has been at the forefront of photochemical and photobiological research in connection with its multifaceted role as a chemical reagent, cytotoxic agent, or messenger in a large variety of processes.[8] Its applications are very diverse ranging from materials science to medicine, with a current uprise in bacterial inactivation and regenerative medicine.[9] $^1O_2$ is generated conveniently by photosensitization, explained in detail in the Supporting Information.[8b,10] In this two-step process, a molecule, referred to as a photosensitizer, absorbs light in the visible or ultraviolet range and transfers its excitation energy to nearby oxygen molecules, which then are promoted to their electronically excited singlet state.[8b,10] Since each of these optical processes can be altered by excited plasmonic nanoparticles, modification in $^1O_2$ generation is expected.[11] Several studies,[11c−e] including our own,[11a] have shown that $^1O_2$ production can be enhanced

near the surface of metallic nanoparticles. However, to the best of our knowledge, the distance dependence of plasmon-enhanced $^1O_2$ production has never been proven for controlled systems where the distance between the $^1O_2$ source and the metallic core is known with certain accuracy. Knowledge of such distance dependence would allow engineering of photosensitizing plasmonic nanomedicines with unprecedented photodynamic efficiency.

Furthermore, $^1O_2$ shows a specific phosphorescence signal at 1275 nm that has been vastly used to gain information on this species with ever-increasing levels of sophistication. Time-resolved $^1O_2$ phosphorescence detection (TRPD or TRNIR) has become the spectroscopic tool of choice for the direct and unambiguous monitoring of $^1O_2$.[12] However, the phosphorescence of $^1O_2$ is extremely weak, with only one in 10^5, or even less, $^1O_2$ molecules decaying by a radiative channel.[13] Since the radiative decay channel is such a minor contribution to the overall $^1O_2$ decay, it could in principle be enhanced, even by orders of magnitude, without introducing any significant distortion in the $^1O_2$ decay kinetics. By consequence, plasmon-enhanced $^1O_2$ emission could result in a significantly more intense phosphorescence signal at 1275 nm than expected from the yield of $^1O_2$, which could boost the sensitivity of $^1O_2$ detection and pave the way to monitor and control the delivery of this important cytotoxic species. To date, a plasmon-enhanced $^1O_2$ phosphorescence signal has only been demonstrated for nanoparticles attached to solid supports.[11b,14] In order to exploit it for biomedical applications it is necessary to translate this phenomenon into biocompatible plasmonic nanomaterials that can be dispersed readily into bulk solution, a goal that has been elusive so far.

In this study, we intend to develop a new plasmonic nanoparticle platform capable of enhancing not only $^1O_2$ production and, therefore, its photodynamic activity, but also $^1O_2$ phosphorescence emission, which would impact our ability to monitor $^1O_2$ in cells and tissue. To achieve this aim, we engineered a series of hybrid silver nanoparticles with a surface bound $^1O_2$ photosensitizer. For the photosensitizer to be influenced by the surface plasmon, it must reside within a specific region near the surface of the metallic nanoparticles at the time of photon absorption (*vide supra*). To this end, silver nanoparticles were coated with a silica shell, acting as a spacer between the metallic core and the photosensitizer. Herein, we synthesized a series of 10 core−shell silver−silica nanoparticles. Each nanoparticle possesses an identical silver core, but presents a different silica shell thickness ranging from 5 to 100 nm. Because the photosensitizer is tethered directly to the silica surface, precise control of the distance separating the photosensitizer from the metallic nanoparticle is achieved at the time of photon absorption. $^1O_2$ production by these hybrid nanoparticles has been investigated by means of both the direct detection of $^1O_2$ phosphorescence emission at 1275 nm and the monitoring of the loss of absorbance of a $^1O_2$ sensor. Plasmonic effects have been assessed with control samples, where the metallic silver core has been removed. Our results demonstrate that the hybrid plasmonic nanoparticles synthesized herein enhance both the production and emission of $^1O_2$ *in vitro*. Most importantly, we show both plasmon-enhanced phenomena to be dependent on proximity to the plasmonic nanostructure, as production and emission of $^1O_2$ experience three regimes as the metallic core moves away from the photosensitizer. Furthermore, we prove these nanomaterials can be delivered to

bacterial cells to boost both their photodynamic antibacterial activity and the detection limit of $^1O_2$ in cells.

RESULTS AND DISCUSSION

Nanoparticle Design. Highly uniform silver nanoparticles (67 ± 7 nm) were prepared by standard citrate reduction (Figure 1).[11a,15] Then, the metallic core was coated successfully via Stöber process with mesoporous silica (Figure 1).[6a,16] As described in the Experimental Section, variation in shell thickness from 5 nm (sample A) to 100 nm (sample J) was achieved by modifying the volume of tetraethylorthosilicate (TEOS) added to the silver core solution. The photosensitizer,
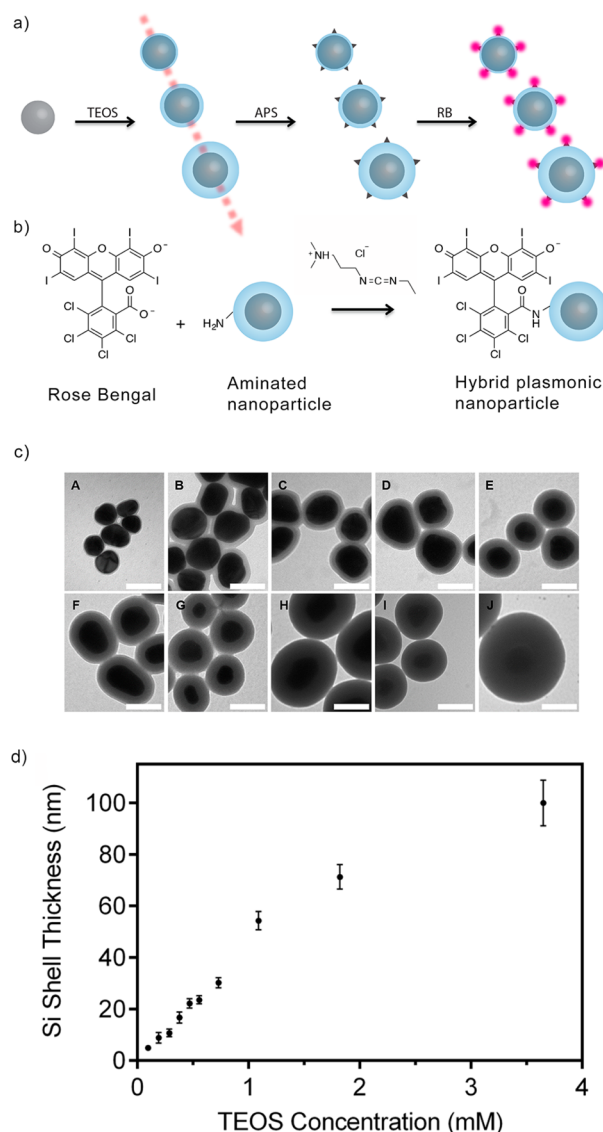

Figure 1. (a) Illustration of the synthetic procedure yielding the hybrid plasmonic nanoparticles with a fixed and controlled distance between the metallic silver core and the photosensitizer Rose Bengal (RB). (b) Illustration of the mechanism to link RB to the surface of the aminated silver−silica nanoparticles by means of carbodiimide coupling chemistry. For simplification, a single amine functional group has been represented on the surface of the nanoparticle. (c) TEM micrographs of the different silver−silica core−shell nanoparticles synthesized in this study. The scale bars represent 100 nm. (d) Plot representing the thickness of the silica shell obtained from TEM images as a function of the TEOS concentration.

Rose Bengal (RB), has a carboxylate moiety allowing for its conjugation to primary amine via standard carbodiimide coupling chemistry (Figure 1).[11a] Therefore, the silica shell was further modified with (3-aminopropyl)triethoxysilane, providing a layer of free amines on the surface of the nanoparticles onto which RB could be tethered (Figure 1).[11a] This controlled arrangement allowed us to study the effect of the metallic silver core at a fixed and controlled distance from the photosensitizer. By choosing RB as the photosensitizer, we not only guaranteed the use of a FDA approved drug with excellent biocompatibility, but we also ensured spectral overlap between the photosensitizer absorption and the plasmon band of the metal nanoparticles, thus enabling the strongest plasmon-enhanced excitation.[6a,11b]

At each stage of synthetic procedure, the nanoparticles were characterized by transmission electron microscopy (TEM) and zeta-potential measurements (see Supporting Information). Figure 1c presents TEM images for the entire series of hybrid plasmonic nanoparticles functionalized with RB, samples A to J. The silica shell thickness was obtained by measuring the distance between the two interfaces silver/silica and silica/vacuum on the TEM images. The reported values are based on measurements performed on an average of 100 nanoparticles. Interestingly, under our experimental conditions, a linear relationship is found between the silica shell thickness and the concentration in TEOS, at least up to a shell thickness of 60 nm (see Figure 1d). Given the concentrations in silver nanoparticles and aminating agent (APS) are identical for each sample synthesized (A to J), it is not surprising the RB surface coverage decreases with increasing nanoparticle's radius (see Supporting Information). It is important to note that this difference in surface coverage will be taken into consideration in the remainder of this study (*vide infra*).

Plasmon-Enhanced $^1O_2$ Generation and Emission In Vitro. $^1O_2$ generation by photosensitization of the hybrid plasmonic nanoparticles was investigated by two independent techniques: the direct detection of $^1O_2$ phosphorescence emission at 1275 nm and the monitoring of the loss of absorbance of the $^1O_2$ sensor ABDA[11a,17] (described in detail in the Supporting Information). Both techniques show the ability of the hybrid plasmonic nanoparticles to generate $^1O_2$ upon visible light irradiation. The presence of the photosensitizer on the nanoparticle's surface is required as hybrid plasmonic nanoparticles lacking photosensitizers are unable to generate $^1O_2$ (see Supporting Information). In other words, the source of $^1O_2$ is the photosensitizer bound to the nanoparticle surface not the silver core or the silica shell.

To assess the impact of the plasmonic core on $^1O_2$ generation, control samples were prepared by removing the silver core from the hybrid plasmonic nanoparticles with chloride ions. This known procedure, referred to as etching, gives rise to hollowed, coreless silica shells.[15,16,18] Successful etching of the hybrid plasmonic nanoparticles, termed etched nanoparticles hereafter, is evaluated by UV–visible absorption spectroscopy as it results in the complete disappearance of the nanoparticle surface plasmon band (see Supporting Information). In the remainder of the study, plasmon-enhanced effect will be assessed for each silica shell thickness by comparing results between the hybrid plasmonic nanoparticles with their specific etched counterpart. Given the hybrid plasmonic nanoparticles and their etched counterparts originate from the same sample, the difference in surface coverage mentioned

in the previous section for the different silica shell thickness has been accounted for.

Time-resolved $^1O_2$ phosphorescence signals, S_t, were acquired for all samples A to J and their etched counterparts and showed the usual rise and decay shape (see Figure 2a and
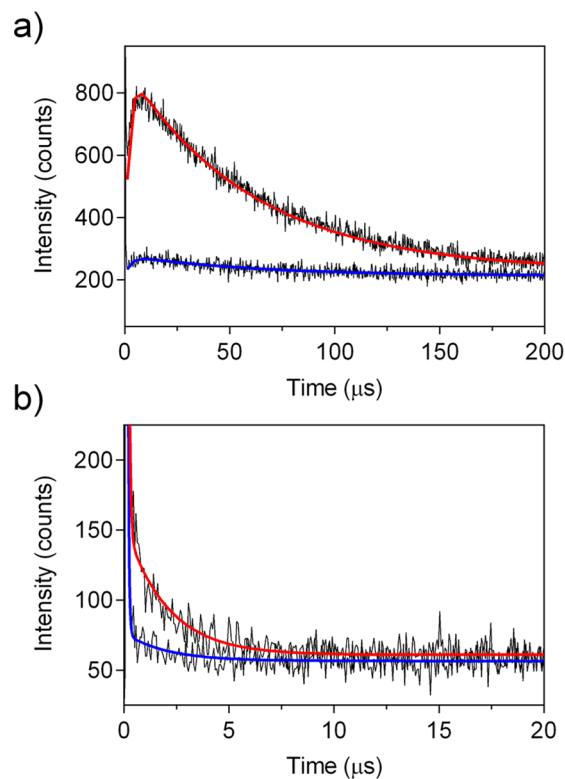

Figure 2. (a) Representative $^1O_2$ time-resolved phosphorescence signal and the corresponding biexponential fittings at 1275 nm for hybrid plasmonic nanoparticles (red) and their etched counterparts (blue) for sample C in air equilibrated D_2O solutions. (b) Representative RB time-resolved phosphorescence signal and the corresponding biexponential fittings at 1110 nm for hybrid plasmonic nanoparticles (red) and their etched counterparts (blue) for sample C in air equilibrated D_2O solutions.

Supporting Information). Inspection of the signals reveals that the silver core exerts a dramatic influence on the intensity of the signal, and that the outcome of such interaction, in turn, depends strongly on the thickness of the silica shell, i.e., the distance between the metal surface and the $^1O_2$ photosensitizer.

These effects were analyzed quantitatively by fitting eq 1[12b] to the phosphorescence data (Figure 2a), which yielded three kinetic parameters, S_0, τ_Δ, and τ_T, corresponding to the signal intensity, the $^1O_2$ decay lifetime, and the RB triplet state lifetime, respectively. The distance between the photosensitizer and the metallic core had no effect on either the triplet RB or the $^1O_2$ lifetime, as the observed values correspond well with those usually found in air-saturated D_2O solutions (see Supporting Information for details).

$$S_t = S_0 \times \frac{\tau_\Delta}{\tau_\Delta - \tau_T}[\exp(-t/\tau_\Delta) - \exp(-t/\tau_T)] \tag{1}$$

In order to compare data from different nanoparticles, an enhancement factor (EF_Δ) was defined as the ratio of S_0 factors of the hybrid plasmonic nanoparticles (Ag@SiO$_2$-RB) relative to those of their etched counterparts (SiO$_2$-RB).

$$EF_\Delta = \frac{S_0^{\text{Ag@SiO}_2\text{-RB}}}{S_0^{\text{SiO}_2\text{-RB}}} \qquad (2)$$

The dependence of EF_Δ on the thickness of the silica shell is shown in Figure 3a. Three distinct regions can be observed. At

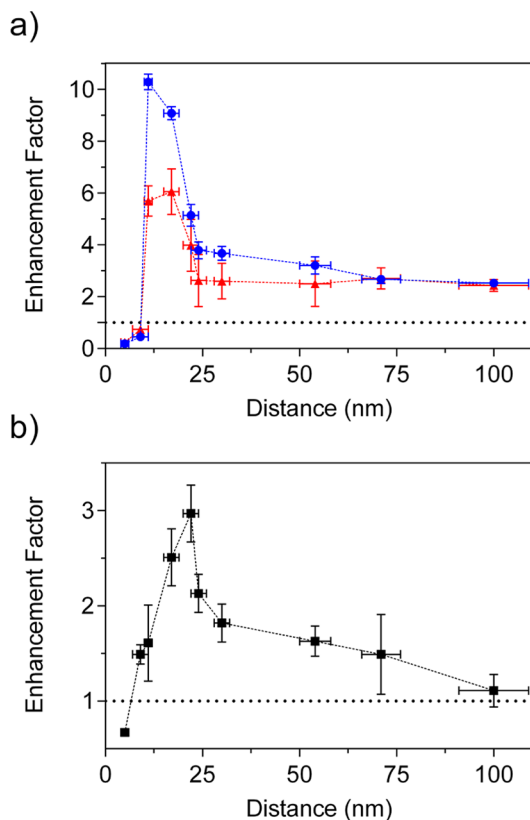**Figure 3.** (a) $^1O_2$ emission (blue circles) and triplet RB enhancement factors (red triangles) as a function of the distance between the metal core and the photosensitizer. The triplet RB enhancement factor is described in the Supporting Information. (b) Enhancement factor for the yield of $^1O_2$ available in solution (black squares) as determined in the Supporting Information.

short distances between the metal and the photosensitizer, the effect of the metal is to quench the $^1O_2$ emission; at intermediate distances, there is an enhancement of the phosphorescence, which passes through a maximum at around 11 nm; finally, the enhancement factor falls at even longer distances and levels off at a value slightly above 1, owing to enhanced light absorption by scattering for the largest particles. While similar behaviors are well documented for plasmon-enhanced fluorescence,[6] this is the first report of distance-dependent plasmon-enhanced $^1O_2$ phosphorescence by metal nanoparticles in suspension where the distance between the metallic core and the photosensitizer is controlled with precision.

Additional insight was obtained from inspection of the phosphorescence of RB at 1110 nm (Figure 2b). This emission originates from the RB triplet state, the immediate $^1O_2$ precursor, and is thus an excellent reporter of the metal influence on $^1O_2$ production. The RB phosphorescence enhancement factors (determined as described in the Supporting Information) are also shown in Figure 3a and follow a similar trend as those for $^1O_2$. It is worth noting that the maximum enhancement factor of the RB phosphorescence

is 40% smaller than that of $^1O_2$ phosphorescence, which indicates that the observed $^1O_2$ phosphorescence enhancement by the silver core is due not only to a higher production of $^1O_2$ but also to an enhancement of its radiative decay. Although the silver nanparticle's plasmon bands show a maximum around 420 nm, this result is not surprising since the local field enhancement is known to extend to the near-infrared.[19] This is the first demonstration that the radiative decay of $^1O_2$ can be enhanced by metal nanoparticles in suspension, all previous observations having been restricted to nanoparticles on solid supports.[11b,14]

A similar distance dependence plot is obtained by the indirect approach, suggesting that the production of $^1O_2$ and its release from the nanoparticles into the solution follow the same trend (Figure 3b). At short photosensitizer−core distance, less $^1O_2$ is generated by the hybrid plasmonic nanoparticles than the control sample, as indicated by an enhancement factor smaller than one (determined as described in the Supporting Information). As the photosensitizer gets farther apart from the silver core, the yield of produced $^1O_2$ is enhanced, reaching a maximum value at a distance around 20 nm. The yield then drops until no enhancement can be detected as judged by an enhancement factor near unity at a distance of 100 nm. Noticeably, some discrepancy exists between the two methodologies, as the maximum enhancement factor is reached at a larger photosensitizer−core distance using the indirect method (Figure 3). As suggested by its name, one has to keep in mind that the approach used in Figure 3b is indirect and $^1O_2$ has to diffuse from the nanoparticle surface to the solution in order to be trapped by the sensor. On the other hand, the observation that $^1O_2$ phosphorescence is also enhanced indicates that the plasmonic structures perturb at least two optical transitions, light absorption by RB ($^1RB^* \leftarrow RB$) and singlet oxygen phosphorescence ($^1O_2 \rightarrow O_2$), which are likely to obey different distance dependence relationships. Therefore, small variations between the two methodologies are to be expected. Nevertheless, maximum enhancement factors observed at distances around 20 nm are in the range of optimal distances reported for other plasmon-enhanced phenomena.[6a,b]

Plasmon-Enhanced $^1O_2$ Generation and Detection in Bacterial Cells. These findings pave the way to the long sought-after goal of boosting the detection limits of $^1O_2$ in cells. We tested this possibility by incubating both Gram-positive *Staphylococcus aureus* cells and Gram-negative *Escherichia coli* as a models with the hybrid plasmonic nanoparticles that showed the maximum enhancement factor (Figure 4). As observed in Figure a,b, a clear $^1O_2$ phosphorescence signal is detected for the hybrid plasmonic nanoparticles, whereas the signal is buried into the noise when the control (etched) nanoparticles are used instead. Since the cells were extensively washed prior to monitoring $^1O_2$ phosphorescence (see Experimental Section), the signal observed in Figure 4a,b cannot be attributed to free nanoparticles present in solution. It originates from nanoparticles either bound or internalized by the bacterial cells.

Furthermore, the enhancement of $^1O_2$ production also increased the ability of hybrid plasmonic nanoparticles to photoinactivate bacteria compared to their etched counterparts and free RB. As shown in Figure 4c, at zero light fluence the nanoparticles themselves exhibit a modest toxicity toward the Gram-positive *S. aureus*. However, the silver core is not responsible for this effect, since the etched nanoparticles show a comparable toxicity. Upon exposure to 20 J·cm^{-2} of green light, free RB and the control etched nanoparticles show,
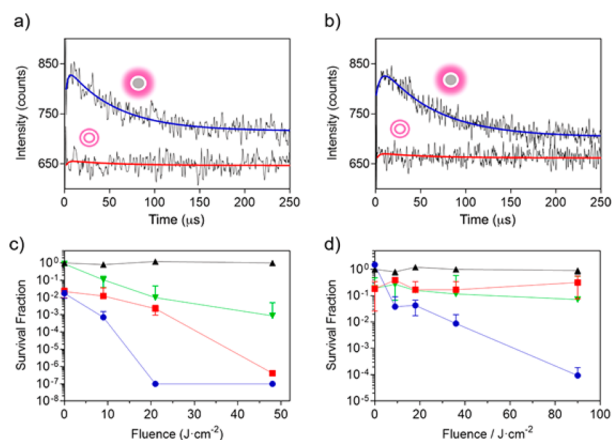
Figure 4. Time-resolved $^1O_2$ phosphorescence signal in air-equilibrated deuterated PBS solutions of *S. aureus* (a) and *E. coli* (b) incubated with hybrid plasmonic nanoparticles and their etched counterpart (λ_{exc} = 532 nm). Survival curves of *S. aureus* (c) and *E. coli* (d) incubated with hybrid plasmonic nanoparticles (blue circles), their etched counterparts (red squares), and free RB at the same concentration (13 μM, green inverted triangles) after being exposed to different light fluences at 530 ± 20 nm. Control experiments (cells without nanoparticles) are represented as black triangles.

respectively, a 2-log$_{10}$ and a 3-log$_{10}$ reduction of the *S. aureus* population (99.9 cell kill), while the optimal hybrid plasmonic nanoparticles (sample C) achieve an impressive 7-log$_{10}$ (99.99999%) colony forming units reduction (Figure 4c). As shown in Figure 4d, no dark toxicity is detected for the hybrid plasmonic nanoparticles toward Gram-negative *E. coli*. Interestingly, upon light exposure, the control etched nanoparticles and free RB do not show improved toxicity toward Gram-negative bacteria even at the highest light fluence tested (Figure 4d). However, the optimal hybrid plasmonic nanoparticles (sample C) achieve a mild 2-log$_{10}$ (99 cell kill) colony forming units reduction upon exposure to 20 J·cm^{-2} of green light, which can be improved to 4-log$_{10}$ reduction of *E. coli* population (99.99 cell kill) at 90 J·cm^{-2} light fluence (Figure 4d). Since Gram-negative bacteria are notoriously difficult to eliminate,[20] the toxicity observed for the hybrid plasmonic nanoparticles toward *E. coli* upon light exposure is quite remarkable. Therefore, these results clearly demonstrate the potential of well-designed plasmonic $^1O_2$ photosensitizers for the photodynamic inactivation of bacteria.

CONCLUSION

The results reported here clearly indicate that precise control can be obtained on the production, photodynamic antibacterial activity, and detection of $^1O_2$ in biological media by careful engineering of plasmonic nanostructures that combine a metal nanoparticle and a $^1O_2$ photosensitizer at well-defined distances. The experiments demonstrate that the silver core exerts a dual role of enhancing both the production of $^1O_2$, through enhanced absorption of light, and its radiative decay, which in turn boosts its detection limit in biological samples. Our findings suggest a strong potential of hybrid plasmonic nanoparticles for theranostic applications.

EXPERIMENTAL SECTION

Synthesis of the Hybrid Plasmonic Nanoparticles. All the chemicals were purchased from Sigma-Aldrich unless otherwise specified.

Synthesis of Silver Nanoparticles. Freshly prepared 39 mM sodium citrate tribasic dihydrate (≥99.0%) aqueous solution (10 mL) was quickly injected into 490 mL of a boiling 1.08 mM silver nitrate (AgNO$_3$, ≥99.0%) solution made in ultrapure water (Milli-Q, 18.2 MΩ cm at 25 °C). The mixture was kept boiling for 1 h and then cooled down to room temperature (RT). Purification was carried out by centrifugation at 47g at RT, and the collected supernatant was brought to a final volume of 350 mL with ultrapure water. The citrate-stabilized silver nanoparticles were kept at 4 °C for a maximum of 2 months.

Synthesis of Silver-Silica Nanoparticles. Addition of a silica layer was performed via a modified Stöber approach. Briefly, 50 mL of the previously prepared silver nanoparticles was diluted in 200 mL anhydrous ethanol containing 4 mL of NH$_4$OH (30 wt%). Using a controlled pressure syringe pump (Fusion 100, Chemyx Inc., Stafford), various volumes of 10 mM tetraethylorthosilicate (TEOS, ≥ 99.0%) solution in anhydrous ethanol were added to the stirred silver nanoparticles solution at a rate of 2.5 mL/h. Following the addition of TEOS, the mixture was allowed to react for 12 h. The nanoparticles were collected by centrifugation at 3000g at RT, washed three times with anhydrous ethanol, and finally suspended in 45 mL of anhydrous ethanol.

Synthesis of Aminated Silver-Silica Nanoparticles. The silica shell is further modified by mixing 20 μL (2 μL/2 min) of 3-aminopropyltriethoxysilane (APS, ≥ 99.0%) with 10 mL silver–silica nanoparticles and stirring at RT overnight. The nanoparticles were then centrifuged at 3000g at RT and washed two times with anhydrous ethanol, followed by one time with 0.1 M 2-(N-morpholino)-ethanesulfonic acid (MES ≥ 99.5%) buffer at pH 6. Finally, the aminated silver−silica nanoparticles were resuspended in 6 mL of 2-(N-morpholino)ethanesulfonic acid (MES) buffer.

Conjugation of the Photosensitizer Onto the Nanoparticle Surface. Thirteen milligrams of 1-ethyl-3-(3-(dimethylamino)-propyl)carbodiimide hydrochloride (EDC, G Biosciences) was dissolved in 6 mL of 5.3 μM Rose Bengal (RB, dye content 93%) in ultrapure water and stirred at RT for 20 min. Then, the 6 mL solution of nanoparticles prepared in the previous section was added to the RB solution and stirred at RT for an additional 3 h in a glass vial wrapped in aluminum foil. The hybrid plasmonic nanoparticles obtained were successively centrifuged and washed with ultrapure water at 3000g, 2625g, and 2250g. The nanoparticles were finally suspended in 6 mL of ultrapure water and kept at 4 °C.

Indirect Detection of Singlet Oxygen. Relative yield of $^1O_2$ generation was obtained by following the disappearance of a water-soluble $^1O_2$ sensor, 9,10-anthracenediyl-bi(methylene)dimalonic acid (ABDA), at 380 nm as a function of irradiation time of the nanoparticle sample.[11a,21] The light source employed in this approach consists of slide projector (Kodak) equipped with an Osram EXR halogen photo optic lamp (300 W, 82 V) and a 480 nm cutoff filter. The absorption of ABDA was measured by means of a UV−visible single-beam spectrophotometer (Cary 50, Varian). All the samples were placed in a semimicro disposable cuvette (1 cm path length). All measurements were performed under ambient atmosphere in ultrapure water unless otherwise specified.

Time-Resolved Near-Infrared Phosphorescence. The specific near-infrared phosphorescence kinetics of triplet Rose Bengal (^{3}RB) and $^1O_2$ were detected by means of a customized PicoQuant Fluotime 200 lifetime system described in detail elsewhere.[12a] Briefly, a diode-pumped pulsed Nd:YAG laser (FTSS355-Q, Crystal Laser, Berlin, Germany) working at 1 kHz repetition rate at 532 nm (12 mW, 1.2 μJ per pulse) was used for excitation. A 1064 nm rugate notch filter (Edmund Optics, York, U.K.) and an uncoated SKG-5 filter (CVI Laser Corporation, Albuquerque, U.S.A.) were placed at the exit port of the laser to remove any residual component of its fundamental emission in the near-infrared (NIR) region. The luminescence exiting from the sample was filtered by a 1100 nm long-pass filter (Edmund Optics, York, U.K.) and narrow bandpass filters at either 1110 nm (BP-1110-070-B, Spectrogon, Sweden) to detect the triplet RB emission, or at 1275 nm (bk-1270-70-B, bk Interfernzoptik, Germany) to isolate the $^1O_2$ emission. A TE-cooled near-IR sensitive photo-

multiplier tube assembly (H9170−45, Hamamatsu Photonics Hamamatsu City, Japan) was used as detector. Photon counting was achieved with a multichannel scaler (NanoHarp 250, PicoQuant Gmbh, Germany). The time-resolved emission decays were analyzed by fitting eq 1 for $^1O_2$ decays or eq 3 in the Supporting Information for ^3RB emission to the data using GraphPad Prism 5. Measurements were carried in air-equilibrated solutions: deuterated water for isolated nanoparticles and deuterated PBS when measuring the luminescence of $^1O_2$ from bacterial cultures.

Microbial Strain and Growth Conditions. *Staphylococcus aureus* CECT 239 and *Escherichia coli* ATCC 25922 were obtained from the Spanish Type Culture Collection (CECT) and the American Type Culture Collection (ATCC), respectively. Bacterial cells were aerobically grown overnight in sterile tryptic soy broth (TSB) at 37 °C to stationary phase. An aliquot was then grown in fresh TSB at 37 °C to an optical density of 0.4 at 600 nm, corresponding to ca. 10^7–10^8 colony-forming units (CFU) per mL. The suspensions were then centrifuged for 10 min at 3000 *g* and resuspended in sterile 0.01 M phosphate buffered saline (PBS, pH 7.4). This procedure was repeated for several cycles.

Photodynamic Inactivation Studies and $^1O_2$ Monitoring. In these experiments, hybrid plasmonic nanoparticles with a silica thickness of 11 nm, corresponding to sample C and referred by this name hereafter, have been employed. Initially, sample C and its etched counterpart were transferred into sterile solutions, which were achieved by centrifugation of the samples at 8000 *g* for 20 min followed by resuspension in sterile PBS. Suspensions of bacteria (10^7 CFU/mL) were then incubated in the dark at room temperature for 30 min with either sample C or its etched counterpart. Care was taken to ensure both nanoparticle suspensions present the same concentration in photosensitizer (1.13 μM in RB). Subsequently, aliquots were removed from each batch and subjected to the same set of different experiments. In one case, the aliquots were employed to monitor $^1O_2$ phosphorescence by means of the system described above. In order to improve the phosphorescence signal and to remove the unbound nanoparticles, the bacterial suspensions were centrifuged at 2000 *g* for 10 min and the pellets were resuspended in 0.01 M deuterated phosphate buffer saline (dPBS). In the other case, the aliquots were used to assess the potential of the nanoparticles for bacterial photoinactivation. For that purpose, the aliquots were placed in 96 well plates, which were illuminated from the top with a green light (Sorisa Photocare, 530 ± 20 nm, 14 mW·cm^{-2} fluence rate). Aliquots were withdrawn from each well at various times during illumination. For determination of CFU, the aliquots were serially diluted, streaked on nutrient agar, and incubated in the dark for 24 h at 37 °C. Controls with light alone and RB (1.13 μM) were additionally performed.

■ ASSOCIATED CONTENT

ⓢ Supporting Information

The Supporting Information is available free of charge on the ACS Publications website at DOI: 10.1021/jacs.5b12704.

> Kinetics of singlet oxygen production and decay in a photosensitized reaction (Scheme S1). Characterization of the nanoparticles: Zeta potential (Figure S1), silica shell thickness (Figure S2), photosensitizer surface coverage (Figure S3). Absorption spectra of the nanoparticles and their etched counterparts (Figure S4). Time-resolved near-infrared phosphorescence signals at 1275 nm (Figure S5). Time-resolved near-infrared phosphorescence signals at 1110 nm (Figure S6). Lifetimes as a function of the distance from the nanoparticles metallic core (Figure S7). Indirect detection of singlet oxygen (Figures S8-S10) (PDF)

■ AUTHOR INFORMATION

Corresponding Authors
*santi.nonell@iqs.url.edu
*bjmheyne@ucalgary.ca

Author Contributions
§N.M., O.P., S.N., and B.H. contributed equally.

Notes
The authors declare no competing financial interest.

■ REFERENCES

(1) (a) Scaiano, J. C.; Stamplecoskie, K. *J. Phys. Chem. Lett.* **2013**, *4*, 1177−1187. (b) Willets, K. A.; Van Duyne, R. P. *Annu. Rev. Phys. Chem.* **2007**, *58*, 267−297. (c) Macia, N.; Heyne, B. *J. Photochem. Photobiol., A* **2015**, *306*, 1−12.

(2) El-Sayed, M. A. *Acc. Chem. Res.* **2001**, *34*, 257−264.

(3) Link, S.; Wang, Z. L.; El-Sayed, M. A. *J. Phys. Chem. B* **1999**, *103*, 3529−3533.

(4) (a) Dragan, A. I.; Bishop, E. S.; Casas-Finet, J. R.; Strouse, R. J.; McGivney, J.; Schenerman, M. A.; Geddes, C. D. *Plasmonics* **2012**, *7*, 739−744. (b) Dragan, A. I.; Geddes, C. D. *Appl. Phys. Lett.* **2012**, *100*, 093115. (c) Zhang, Y.; Aslan, K.; Previte, M. J. R.; Malyn, S. N.; Geddes, C. D. *J. Phys. Chem. B* **2006**, *110*, 25108−25114.

(5) Liau, Y.-H.; Unterreiner, A. N.; Chang, Q.; Scherer, N. F. *J. Phys. Chem. B* **2001**, *105*, 2135−2142.

(6) (a) Abadeer, N. S.; Brennan, M. R.; Wilson, W. L.; Murphy, C. J. *ACS Nano* **2014**, *8*, 8392−8406. (b) Cheng, D.; Xu, Q.-H. *Chem. Commun.* **2007**, 248−250. (c) Mishra, H.; Mali, B. L.; Karolin, J.; Dragan, A. I.; Geddes, C. D. *Phys. Chem. Chem. Phys.* **2013**, *15*, 19538−19544. (d) Pompa, P. P.; Martiradonna, L.; Della Torre, A.; Della Sala, F.; Manna, L.; De Vittorio, M.; Calabi, F.; Cingolani, R.; Rinaldi, R. *Nat. Nanotechnol.* **2006**, *1*, 126−130.

(7) Anger, P.; Bharadwaj, P.; Novotny, L. *Phys. Rev. Lett.* **2006**, *96*, 113002.

(8) (a) DeRosa, M. C.; Crutchley, R. J. *Coord. Chem. Rev.* **2002**, *233*−234, 351−371. (b) Ogilby, P. R. *Chem. Soc. Rev.* **2010**, *39*, 3181−3209.

(9) (a) Jori, G.; Camerin, M.; Soncin, M.; Guidolin, L.; Coppellotti, O.*Photodynamic Inactivation of Microbial Pathogens: Medical and Environmental Applications*; RSC Publishing: Cambridge, 2011. (b) Austen, W. G.; McCormack, M.; Redmond, R. W.; Kochevar, I. E.*Methods for Tissue Passivation*. U.S. Patent WO2014015274A1, 2014.

(10) Wilkinson, F.; Helman, W. P.; Ross, A. B. *J. Phys. Chem. Ref. Data* **1993**, *22*, 113−262.

(11) (a) Mooi, S. M.; Heyne, B. *Photochem. Photobiol.* **2014**, *90*, 85−91. (b) Toftegaard, R.; Arnbjerg, J.; Daasbjerg, K.; Ogilby, P. R.; Dmitriev, A.; Sutherland, D. S.; Poulsen, L. *Angew. Chem., Int. Ed.* **2008**, *47*, 6025−6027. (c) Zhang, Y.; Aslan, K.; Previte, M. J. R.;

Geddes, C. D. *Proc. Natl. Acad. Sci. U. S. A.* **2008**, *105*, 1798−1802. (d) Hu, B.; Cao, X.; Nahan, K.; Caruso, J.; Tang, H.; Zhang, P. *J. Mater. Chem. B* **2014**, *2*, 7073−7081. (e) Ke, X.; Wang, D.; Chen, C.; Yang, A.; Han, Y.; Ren, L.; Li, D.; Wang, H. *Nanoscale Res. Lett.* **2014**, *9*, 666.

(12) (a) Jimenez-Banzo, A.; Ragas, X.; Kapusta, P.; Nonell, S. *Photochem. Photobiol. Sci.* **2008**, *7*, 1003−1010. (b) Nonell, S.; Braslavsky, S. E. *Methods Enzymol.* **2000**, *319*, 37−49. (c) Wu, H.; Song, Q.; Ran, G.; Lu, X.; Xu, B. *TrAC, Trends Anal. Chem.* **2011**, *30*, 133−141.

(13) (a) Kanofsky, J. R. *Photochem. Photobiol.* **2011**, *87*, 14−17. (b) Hasebe, N.; Suzuki, K.; Horiuchi, H.; Suzuki, H.; Yoshihara, T.; Okutsu, T.; Tobita, S. *Anal. Chem.* **2015**, *87*, 2360−2366.

(14) Ragas, X.; Gallardo, A.; Zhang, Y.; Massad, W.; Geddes, C. D.; Nonell, S. *J. Phys. Chem. C* **2011**, *115*, 16275−16281.

(15) Lessard-Viger, M.; Rioux, M.; Rainville, L.; Boudreau, D. *Nano Lett.* **2009**, *9*, 3066−3071.

(16) L.-Viger, M.; Brouard, D.; Boudreau, D. *J. Phys. Chem. C* **2011**, *115*, 2974−2981.

(17) Aubry, J.-M.; Pierlot, C.; Rigaudy, J.; Schmidt, R. *Acc. Chem. Res.* **2003**, *36*, 668−675.

(18) Yang, J.; Aschemeyer, S.; Martinez, H. P.; Trogler, W. C. *Chem. Commun.* **2010**, *46*, 6804−6806.

(19) (a) Radziuk, D.; Moehwald, H. *Phys. Chem. Chem. Phys.* **2015**, *17*, 21072−21093. (b) Tanabe, K. *J. Phys. Chem. C* **2008**, *112* (40), 15721−15728.

(20) (a) Maisch, T.; Baier, J.; Franz, B.; Maier, M.; Landthaler, M.; Szeimies, R.-M.; Baumler, W. *Proc. Natl. Acad. Sci. U. S. A.* **2007**, *104*, 7223−7228. (b) Malik, Z.; Ladan, H.; Nitzan, Y. *J. Photochem. Photobiol., B* **1992**, *14*, 262−6. (c) Banks, J. G.; Board, R. G.; Carter, J.; Dodge, A. D. *J. Appl. Bacteriol.* **1985**, *58*, 391−400. (d) Dahl, T. A.; Midden, W. R.; Neckers, D. C. *Photochem. Photobiol.* **1988**, *48*, 607−12.

(21) Hoebeke, M.; Damoiseau, X. *Photochem. Photobiol. Sci.* **2002**, *1*, 283−287.